Epitaxial Growth of Honeycomb Monolayer CuSe with Dirac Nodal Line Fermions

Lei Gao, Jia-Tao Sun, Jian-Chen Lu, Hang Li, Kai Qian, Shuai Zhang, Yu-Yang Zhang, Tian Qian, Hong Ding, Xiao Lin,* Shixuan Du,* and Hong-Jun Gao

2D transition metal chalcogenides have attracted tremendous attention due to their novel properties and potential applications. Although 2D transition metal dichalcogenides are easily fabricated due to their layer-stacked bulk phase, 2D transition metal monochalcogenides are difficult to obtain. Recently, a single atomic layer transition metal monochalcogenide (CuSe) with an intrinsic pattern of nanoscale triangular holes is fabricated on Cu(111). The first-principles calculations show that free-standing monolayer CuSe with holes is not stable, while hole-free CuSe is endowed with the Dirac nodal line fermion (DNLF), protected by mirror reflection symmetry. This very rare DNLF state is evidenced by topologically nontrivial edge states situated inside the spin–orbit coupling gaps. Motivated by the promising properties of hole-free honeycomb CuSe, monolayer CuSe is fabricated on Cu(111) surfaces by molecular beam epitaxy and confirmed success with high resolution scanning tunneling microscopy. The good agreement of angle resolved photoemission spectra with the calculated band structures of CuSe/Cu(111) demonstrates that the sample is monolayer CuSe with a honeycomb lattice. These results suggest that the honeycomb monolayer transition metal monochalcogenide can be a new platform to study 2D DNLFs.

2D materials are important in optoelectronics, catalysts, sensors, energy storage, etc., due to their large specific surface area and novel properties.[1–12] Among them, transition metal chalcogenides (TMCs) have attracted the most attention, owing to their novel properties (which differ from the bulk properties) and the consequent prospective applications.[13–22] Unlike 2D transition metal dichalcogenides (TMDs), which are naturally layered in their bulk phase, most transition metal monochalcogenides (TMMs) are not layered, making 2D TMMs difficult to obtain. Due to the special properties of monolayer honeycomb

L. Gao, Dr. J.-T. Sun, Dr. J.-C. Lu, H. Li, K. Qian, S. Zhang, Dr. Y.-Y. Zhang, Prof. T. Qian, Prof. H. Ding, Prof. X. Lin, Prof. S. X. Du, Prof. H.-J. Gao
Institute of Physics
Chinese Academy of Sciences
Beijing 100190, P. R. China
E-mail: xlin@ucas.ac.cn; sxdu@iphy.ac.cn

L. Gao, Dr. J.-T. Sun, Dr. J.-C. Lu, H. Li, K. Qian, S. Zhang, Dr. Y.-Y. Zhang, Prof. T. Qian, Prof. H. Ding, Prof. X. Lin, Prof. S. X. Du, Prof. H.-J. Gao
University of Chinese Academy of Sciences
Chinese Academy of Sciences
Beijing 100190, P. R. China

The ORCID identification number(s) for the author(s) of this article can be found under https://doi.org/10.1002/adma.201707055.

lattice,[23–29] 2D TMMs with such a lattice attract much interest. Recently, we successfully fabricated honeycomb monolayer CuSe on Cu(111) surfaces.[30] However, the monolayer CuSe is a patterned layer with intrinsic nanoscale triangular holes induced by the lattice mismatch between CuSe and the substrate. It is natural to ask what intrinsic electronic properties honeycomb monolayer CuSe could have and whether honeycomb monolayer CuSe could be synthesized without nanoscale holes. Further research is much needed to consistently understand this new 2D material, planar (PL) honeycomb CuSe, via both theory and experiment.

Here, we report a monolayer CuSe with a 1D moiré pattern, rather than the patterned triangular holes, successfully fabricated by direct selenization of Cu(111) at low Se coverage. A honeycomb lattice is observed in the sample via high resolution scanning tunneling microscopy (STM). First-principles calculations studied together with angle resolved photoemission spectroscopy (ARPES) spectra demonstrate that our sample is monolayer CuSe with a distorted honeycomb lattice on Cu(111). Further calculations based on a free-standing monolayer CuSe predict that planar CuSe with a honeycomb lattice possesses two 2D Dirac nodal line fermions (DNLFs) protected by mirror reflection symmetry (MRS). The two 2D DNLFs are contributed by Se 4p and Cu 3d orbitals around the Γ point without considering the spin–orbit coupling (SOC). When SOC is included, the model shows topological edge states inside the gaps of the two nodal line rings. Our calculations demonstrate that monolayer CuSe on a weakly coupled substrate like graphene could be a candidate 2D material with DNLFs.
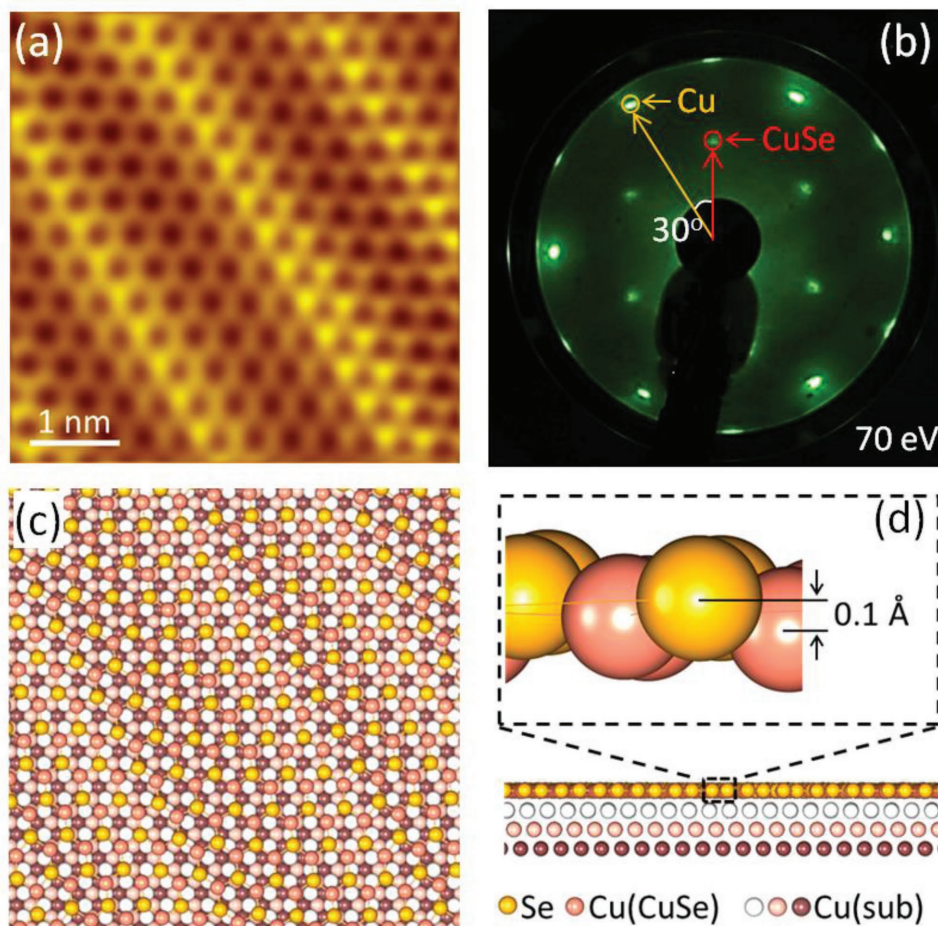
Figure 1a shows a high-resolution STM image of monolayer CuSe on Cu(111), which were grown by a straightforward precursor-free method, that is, through a single step of direct selenization on Cu(111) substrate. Because of the uniaxially distorted honeycomb structure of monolayer CuSe with respect to the Cu(111) surface (see Figure S1, Supporting Information, for details), 1D moiré patterns are clearly observed. We observed three kinds of monolayer CuSe domains distinguished by the symmetry of the Cu(111) (see Figures S2 and S3, Supporting Information, for details), which would have significant influence on the constant energy contours (CECs) discussed below.

Figure 1. Atomic configuration and LEED pattern of monolayer CuSe on Cu(111). a) High-resolution STM image ($V_s = -137$ mV, $I_t = 0.1$ nA). b) LEED pattern. The red and yellow circles indicate the diffraction spots in the CuSe and Cu(111) lattices, respectively. The rotation between lattices is 30°. c,d) Top view (c) and side view (d) of the optimized atomic structure of monolayer CuSe on Cu(111), with a 1D moiré pattern.

The low energy electron diffraction (LEED) pattern in Figure 1b shows a rotation of 30° between the monolayer CuSe and the Cu(111) surface but with uniaxial displacement of pattern. This further supports the uniaxial distortion between them along one of the three equivalent directions in strain free form.

To investigate the atomic configuration of monolayer CuSe on Cu(111) surface, we built a slab model in a large supercell of 38.27 × 4.25 Å, shown in Figure S4 in the Supporting Information. Figure 1c,d is top and side views of the relaxed model of monolayer CuSe on Cu(111). We found that the calculated results show a 1D moiré pattern which is in good agreement with the experimental STM observation in Figure 1a. The calculated maximal buckling height of the monolayer CuSe on Cu(111) surface is 0.1 Å, consistent with the height difference in the STM topographic image (Figure S1, Supporting Information). The average separation between the monolayer CuSe and the Cu(111) surface is 2.05 Å, rendering mechanical exfoliation of the monolayer CuSe from the Cu surface very difficult.

To investigate the electronic structures of monolayer CuSe, we carried out ARPES measurements by transferring the samples with a high-vacuum suitcase from the molecular beam epitaxial chamber. **Figure 2**a shows experimental band dispersions

along the K–Γ–K direction of the Brillouin zone of monolayer CuSe. We observe two hole-like bands at energy above −2 eV and intensive electronic density of states at energy below −2 eV, which is known to be contributed by the Cu(111) substrate. To understand the experiments, we performed first-principles calculation on the uniaxially distorted monolayer CuSe on a ten-layer Cu(111) substrate with the spin–orbital coupling (SOC) effect included. To alleviate the large computation expense encountered when using a unit cell observed in STM experiments (Figure S4, Supporting Information), a (1 × 1) unit cell of monolayer CuSe on Cu(111) is used here. Figure 2b shows two hole-like bands with large splitting in the projected band structures of the monolayer CuSe, denoted by red dashed lines—the band dispersion below −2 eV is contributed by the bulk Cu. The calculated band structure in Figure 2b well reproduces the ARPES results.

In Figure 2c,d, we show constant energy contours (CECs) at the binding energies of −0.440 and −0.875 eV, respectively. The Brillouin zones of CuSe and Cu(111) are marked by red and yellow dashed lines respectively in Figure 2c. The high intensity at $k_x \approx 1.0$ Å^{-1} in Figure 2c comes from the electron band of Cu(111) substrate.[31] The CECs at binding energy of −0.875 eV
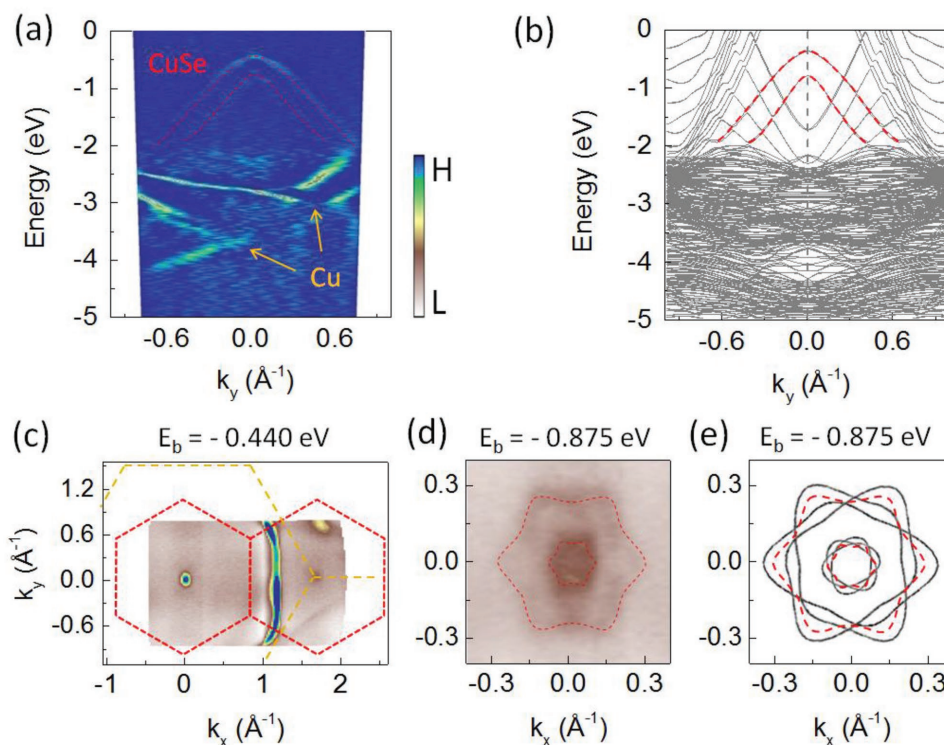
Figure 2. ARPES and calculation results of monolayer CuSe on Cu(111). a) ARPES intensity plots measured along the K–Γ–K direction. b) Calculated band structure with SOC. The two hole-like bands of monolayer CuSe are denoted by the red lines in both panels. c) Experimental constant energy contours (CECs) taken at $E_b = -0.440$ eV. The Brillion zones of CuSe and Cu(111) are denoted by the red and yellow dashed lines, respectively. d) Experimental CECs taken at $E_b = -0.875$ eV. e) The black lines are the calculated CECs at $E_b = -0.875$ eV considering three equivalent domains of uniaxially distorted CuSe on Cu(111). The experimental CECs are superimposed as red dashed lines.

show two hexagrams centered at the Γ point, marked by red dashed lines in Figure 2d. The calculated CECs at −0.875 eV show a C_2 symmetry due to the uniaxial distortion (Figure S5b, Supporting Information). Considering the size of each domain (≈100 nm) is much smaller than that of the spot diameter of ARPES (≈3 mm), the band information of all three equivalent domains are collected during the APRES characterization of CuSe/Cu(111) sample. Therefore, the calculated CECs are believed to be the superposition of the CECs of these three domains (the black lines in Figure 2e and Figure S5c, Supporting Information). The superposition of CECs also shows hexagram like structures, consistent with the ARPES measurements in Figure 2d. The consistent features from ARPES and STM measurements support that the sample is indeed monolayer CuSe on Cu(111).

In order to further investigate the intrinsic electronic properties of monolayer CuSe, we use a free-standing CuSe monolayer model to avoid the influence of the substrate. We varied the lattice parameters to look for possible configurations with local energy minima. Two kinds of atomic structures are found in free-standing monolayer CuSe—the low-buckled (LB) phase (**Figure 3**a) and the PL phase. We found that the fully relaxed PL phase is more stable than the LB phase (upper panel of Figure 3b). The PL phase is a thermodynamically stable state according to the phonon dispersion calculation, as shown in Figure 3d. Because of the presence of imaginary frequencies in the phonon dispersion (Figure 3c), the LB phase is not a stable

phase. The evolution of the buckling heights with the in-plane lattice parameters shows an abrupt decrease between LB and PL phases (lower panel of Figure 3b). The point groups for the LB and PL phase are C_{3v} and D_{3h}, respectively, both of which have MRS with respect to the yz plane (M_{yz}) as shown in Figure 3a. The main difference between them in crystalline symmetry is MRS with respect to the xy plane (M_{xy}).

The calculated band structure without SOC for the PL phase is shown in **Figure 4**a. The three bands in the energy range of −2 eV away from the vicinity of the Fermi level are denoted by α, β, and γ. Projected band structures for the PL phase (refer to Figure S6, Supporting Information, for more detail) show that three bands can be classified into two groups, where α/β and γ bands are dominated by in-plane (Se p_x/p_y and Cu $d_{xy}/d_{x^2-y^2}$) and out-of-plane (Se p_z and Cu d_{xz}/d_{yz}) orbitals, respectively. It is interesting to note that, for the PL phase, the γ band crosses both α and β bands linearly at the touching points without opening energy gaps like the massless Dirac fermion of graphene. We found that the little group for the PL phase along the Γ–K direction is C_s with mirror reflection symmetry M_{xy}, where the irreducible representations (IRs) for α, β, γ bands are A′, A′, and A″, respectively. The little group for the PL phase along the Γ–M direction is C_{2v} with mirror reflection symmetries M_{yz} and M_{xy}, where the IRs for α, β, γ bands are A₁, B₁ and B₂, respectively. Since the IRs A′, A₁, B₁ under mirror reflection symmetry M_{xy} operations are even, the mirror parities for the α/β bands are even, as indicated by "+." The mirror parity for
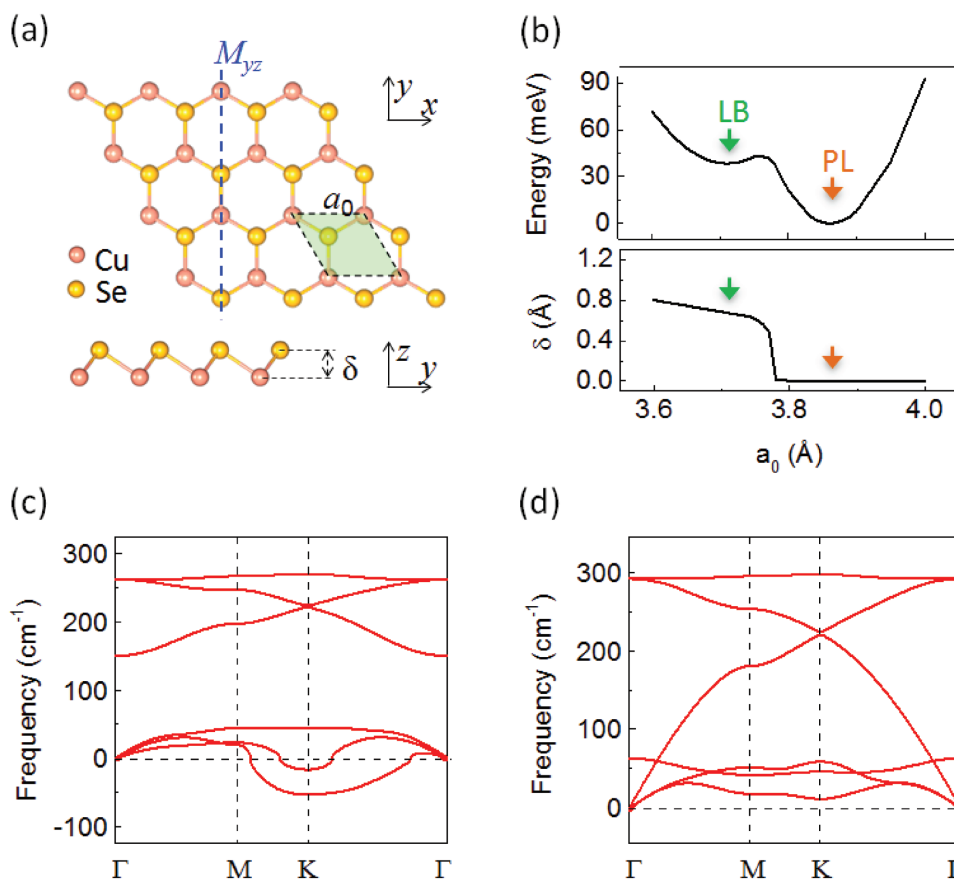
Figure 3. Atomic configuration and stability of monolayer CuSe. a) Top and side views. The mirror reflection symmetry M_{yz} is denoted by the blue dashed line. b) Relative energies and buckling height δ as functions of the lattice parameter a_0. The low-buckled (LB) phase and the planar (PL) phase are denoted by green arrows and orange arrows, respectively. The energies are referenced to that of the PL phase. c,d) Phonon dispersions for the LB phase (c) and the PL phase (d).

the γ band is opposite to those of the α, β bands, as indicated by "−." The opposite mirror parity ensures the emergence of these two DNLFs protected by mirror reflection symmetry M_{xy}, as shown in Figure 4b.

To investigate the topological properties of the DNLF, an energy gap opening is required around these crossings if the mirror reflection symmetry M_{xy} is broken. This can be achieved via the atomic buckling or SOC because of the weak coupling of the in-plane and out-of-plane orbitals. We take the calculated band structure of PL CuSe with SOC shown in Figure 4c as an example. In this case, the opened gaps along the M–Γ–K direction are 89, 63, 50, and 90 meV, respectively. Then we construct an effective tight-binding Hamiltonian in the maximally localized Wannier function (see the Experimental Section). The edge states of semi-infinite monolayer CuSe with Se-terminated zigzag edge without any edge saturation were obtained by the iterative Green's function method, as shown in Figure 4d. In addition to the topologically trivial edge states from the edge dangling bond outside the gap, we can clearly see the topologically nontrivial edge states (denoted by orange and blue dashed circles) inside the gap of the two DNLFs around the Γ point. Interestingly, the Rashba-type topologically nontrivial edge states at the energy of −1.1 eV indicates asymmetric potential across the edge because of the absence of inversion symmetry. One can clearly observe

that the real-space charge density of both nodal line (NL) edge states in the Brillouin zone center shown in Figures S7 and S8 in the Supporting Information are localized at Cu and Se edges. The emergence of NL edge states is independent on the hydrogen saturation along the nanoribbon edge manifesting its nontrivial nature (see the discussion in the Supporting Information).

In order to further investigate symmetry-protected properties of the two nodal line rings, we considered the atomic buckling. Even very small atomic buckling height eliminates the mirror reflection symmetry M_{xy}, thus annihilating the Dirac nodal line rings by opening gaps at some of the band-crossing points. The behaviors of these crossing points of PL CuSe along Γ–M and Γ–K directions with different buckling heights are shown in Figure S9 in the Supporting Information. When buckling height is low, one of the two nodal line rings will open gaps while the other one will form Dirac cones along the Γ–M directions. The different IRs of the β (A″) and γ (A′) bands along the Γ-M direction ensure that the crossing point is a Dirac cone protected by mirror reflection symmetry M_{yz}. As the buckling height δ increases, the out-of-plane coupling between Se p_z and Cu d_{xz}/d_{yz} is weakened, resulting in a narrowed energy band width of the β and γ bands along the Γ–M direction. When buckling height is greater than 0.6 Å, both of the nodal line rings will be fully gapped.
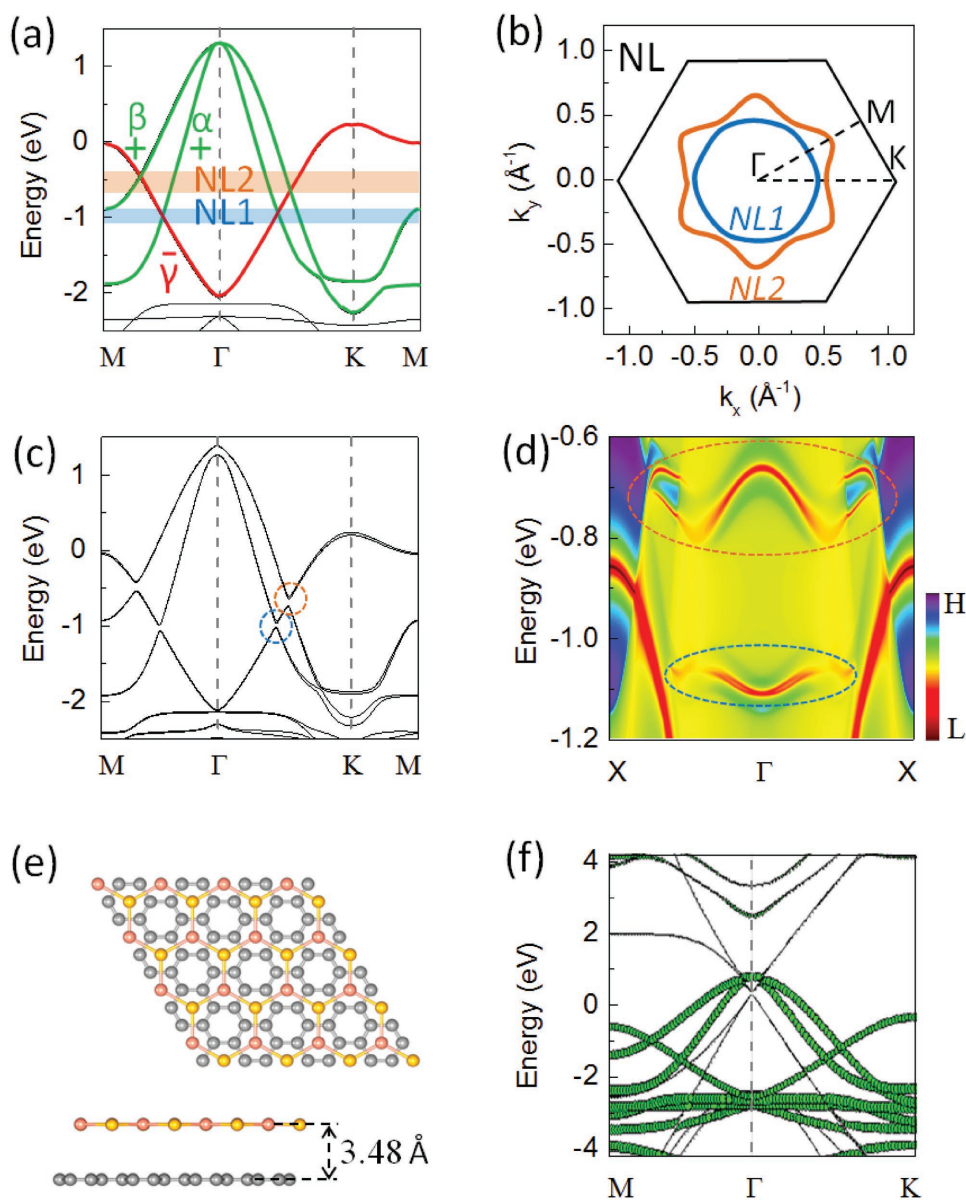
Figure 4. Calculated electronic structures of the PL phase of monolayer CuSe. a) Projected band structure of a free-standing monolayer CuSe in PL phase without SOC. The α and β band contributed by in-plane orbitals Se p_x/p_y and Cu $d_{xy}/d_{x^2-y^2}$ are denoted by green lines. The γ band contributed by the out-of-plane orbitals Se p_z and Cu d_{xz}/d_{yz} is denoted by red line. b) Momentum distributions at the blue and orange shaded regions in (a) of the nodal line rings: NL1 and NL2, respectively. c) Band structure of a free-standing monolayer CuSe in PL phase considering SOC. d) Edge states of semi-infinite CuSe with Se-terminated zigzag edges denoted by orange and blue dashed circles, which corresponded to those in (c). e) Top and side views of a configuration of monolayer CuSe on graphene. f) Projected band structure of monolayer CuSe on graphene without SOC.

It has been shown in Figure 2a that the ARPES experiment on CuSe/Cu(111) did not observe the band crossing between the α/β and γ bands. The reason is that the strong coupling between out-of-plane orbitals of CuSe and the Cu(111) annihilates the γ band. Therefore, DNLFs do not appear when monolayer CuSe is grown on Cu(111). We then calculate the band structure of monolayer CuSe on weakly coupled graphene with an interlayer separation of 3.48 Å (Figure 4e). The band crossing of monolayer CuSe remains as demonstrated by the projected band structures on CuSe, confirming the emergence of DNLFs (Figure 4f). We propose that the monolayer CuSe

has great potential to be a candidate of producing intriguing DNLFs provided that planar CuSe monolayer is synthesized on a weakly interacting substrate such as graphene. We noted that a recent publication claimed the observation of the DNLFs of monolayer Cu$_2$Si on a weakly coupled substrate.[32]

In summary, monolayer CuSe epitaxially grown on Cu(111) surfaces has been investigated by STM, ARPES, and first-principles calculation. We found the emergence of mirror reflection symmetry-protected DNLFs in free-standing monolayer CuSe, dominated by the Se 4p and Cu 3d orbitals, making the monolayer CuSe a candidate for 2D DNLF. The nontrivial

**ADVANCED
SCIENCE NEWS**

www.advancedsciencenews.com

**ADVANCED
MATERIALS**

www.advmat.de

topological edge states further evidence our proposal if the mirror reflection symmetry is broken by SOC or atomic buckling. Using first-principles calculation, we theoretically predict that the intriguing DNLF properties can be directly observed using ARPES if monolayer CuSe can be synthesized on weakly coupled substrate, such as graphene. Furthermore, 2D materials with 1D moiré pattern have been reported to host array of 1D topological mode at the smooth interfaces between local regions of distinct topological properties across the moiré.[33] Since the planar monolayer CuSe hosts the gapless Dirac nodal line spectrum, which is at the critical point between two topologically distinct gapped spectra, the 1D moiré superlattice, which is likely to host both type of gapped spectra at different local regions, is probably exhibiting arrays of 1D topological interface modes.

Experimental Section

First-Principles Calculations: First-principles calculations are performed using the Vienna ab initio simulation package.[34,35] The local density approximation[36] is used for exchange and correlation. The electron wavefunctions are expanded in plane wave basis with a kinetic energy cutoff of 450 eV. In the calculations of free-standing monolayer CuSe, a 15 Å vacuum layer is used, and all atoms are fully relaxed until the residual forces on each atom are smaller than 10^{-3} eV Å^{-1}. The k-points sampling is $39 \times 39 \times 1$ with the Gamma scheme. A slab model of monolayer CuSe on top of Cu(111) surface is used to simulate the interfacial interaction between them by employing a larger supercell of 38.27 Å $\times$ 4.25 Å. The five Cu d orbitals and three Se p orbitals are used to construct the maximally localized Wannier function.[37–40] Phonon dispersion is calculated based on a 6×6 supercell in the finite displacement method as implemented in the PHONOPY package.[41–43]

Sample Preparation, STM Measurement, and ARPES Measurement: The monolayer CuSe was grown in a commercial ultrahigh vacuum system (Omicron) with a base pressure better than 1×10^{-10} mbar. The clean single-crystal Cu(111) (MaTeck) surface was obtained via cycles of argon-ion sputtering followed by annealing at 550 °C. High-purity Se (99.99%, Sigma-Aldrich) evaporated from a Knudsen cell (125 °C for 20 min) was deposited onto the clean Cu(111) surface at room temperature. After preparation, the samples were transferred to the low-temperature STM head operating at ≈4 K and the ARPES chamber, without breaking the vacuum. STM images of the monolayer CuSe were acquired in the constant-current mode, using an electrochemically etched tungsten tip. All voltages were applied to the sample with respect to the tip. The Nanotec Electronica WSxM software was used to process the STM images.[44] During ARPES measurement, the sample was kept at 30 K. Energy resolution was better than 30 meV. Pressure during measurements was below 4×10^{-11} mbar.

Supporting Information

Supporting Information is available from the Wiley Online Library or from the author.

Acknowledgements

Conflict of Interest

The authors declare no conflict of interest.

Keywords

[1] A. H. Castro Neto, F. Guinea, N. M. R. Peres, K. S. Novoselov, A. K. Geim, *Rev. Mod. Phys.* **2009**, *81*, 109.

[2] J.-L. Lu, W. Luo, X.-Y. Li, S.-Q. Yang, J.-X. Cao, X.-G. Gong, H.-J. Xiang, *Chem. Phys. Lett.* **2017**, *34*, 057302.

[3] C. R. Woods, L. Britnell, A. Eckmann, R. S. Ma, J. C. Lu, H. M. Guo, X. Lin, G. L. Yu, Y. Cao, R. V. Gorbachev, A. V. Kretinin, J. Park, L. A. Ponomarenko, M. I. Katsnelson, Y. N. Gornostyrev, K. Watanabe, T. Taniguchi, C. Casiraghi, H. J. Gao, A. K. Geim, K. S. Novoselov, *Nat. Phys.* **2014**, *10*, 451.

[4] P. Y. Chen, M. Liu, Z. Wang, R. H. Hurt, I. Y. Wong, *Adv. Mater.* **2017**, *29*, 1605096.

[5] J. Deng, D. Deng, X. Bao, *Adv. Mater.* **2017**, *29*, 1606967.

[6] P. Miro, M. Audiffred, T. Heine, *Chem. Soc. Rev.* **2014**, *43*, 6537.

[7] C. Tan, Z. Lai, H. Zhang, *Adv. Mater.* **2017**, *29*, 1701392.

[8] M. Xu, T. Liang, M. Shi, H. Chen, *Chem. Rev.* **2013**, *113*, 3766.

[9] P. Ares, J. J. Palacios, G. Abellan, J. Gomez-Herrero, F. Zamora, *Adv. Mater.* **2017**, *29*, 1703771.

[10] S. Y. Cho, Y. Lee, H. J. Koh, H. Jung, J. S. Kim, H. W. Yoo, J. Kim, H. T. Jung, *Adv. Mater.* **2016**, *28*, 7020.

[11] V. P. Pham, G. Y. Yeom, *Adv. Mater.* **2016**, *28*, 9024.

[12] S. Yu, X. Wu, Y. Wang, X. Guo, L. Tong, *Adv. Mater.* **2017**, *29*, 1606128.

[13] M. Acerce, D. Voiry, M. Chhowalla, *Nat. Nanotechnol.* **2015**, *10*, 313.

[14] K. Chen, X. Wan, W. Xie, J. Wen, Z. Kang, X. Zeng, H. Chen, J. Xu, *Adv. Mater.* **2015**, *27*, 6431.

[15] L. Fu, F. Wang, B. Wu, N. Wu, W. Huang, H. Wang, C. Jin, L. Zhuang, J. He, L. Fu, Y. Liu, *Adv. Mater.* **2017**, *29*, 1700439.

[16] A. Gurarslan, S. Jiao, T. D. Li, G. Li, Y. Yu, Y. Gao, E. Riedo, Z. Xu, L. Cao, *Adv. Mater.* **2016**, *28*, 10055.

[17] D. H. Keum, S. Cho, J. H. Kim, D.-H. Choe, H.-J. Sung, M. Kan, H. Kang, J.-Y. Hwang, S. W. Kim, H. Yang, K. J. Chang, Y. H. Lee, *Nat. Phys.* **2015**, *11*, 482.

[18] K. F. Mak, J. Shan, *Nat. Photonics* **2016**, *10*, 216.

[19] J. Ping, Z. Fan, M. Sindoro, Y. Ying, H. Zhang, *Adv. Funct. Mater.* **2017**, *27*, 1605817.

[20] S. M. Huang, S. Y. Xu, I. Belopolski, C. C. Lee, G. Chang, B. Wang, N. Alidoust, G. Bian, M. Neupane, C. Zhang, S. Jia, A. Bansil, H. Lin, M. Z. Hasan, *Nat. Commun.* **2015**, *6*, 7373.

[21] Y. Zhang, B. Zheng, C. Zhu, X. Zhang, C. Tan, H. Li, B. Chen, J. Yang, J. Chen, Y. Huang, L. Wang, H. Zhang, *Adv. Mater.* **2015**, *27*, 935.

[22] Q. Lu, Y. Yu, Q. Ma, B. Chen, H. Zhang, *Adv. Mater.* **2016**, *28*, 1917.

[23] M. Ezawa, *Phys. Rev. Lett.* **2012**, *109*, 055502.

[24] J. Li, L. Niu, Z. Zheng, F. Yan, *Adv. Mater.* **2014**, *26*, 5239.

[25] C.-X. Liu, S.-C. Zhang, X.-L. Qi, *Annu. Rev. Condens. Matter Phys.* **2016**, *7*, 301.

[26] H. Pan, Z. Li, C. C. Liu, G. Zhu, Z. Qiao, Y. Yao, *Phys. Rev. Lett.* **2014**, *112*, 106802.

[27] Y. Ren, J. Zeng, X. Deng, F. Yang, H. Pan, Z. Qiao, *Phys. Rev. B* **2016**, *94*, 085411.

[28] N. O. Weiss, H. Zhou, L. Liao, Y. Liu, S. Jiang, Y. Huang, X. Duan, *Adv. Mater.* **2012**, *24*, 5782.

[29] W. F. Tsai, C. Y. Huang, T. R. Chang, H. Lin, H. T. Jeng, A. Bansil, *Nat. Commun.* **2013**, *4*, 1500.

[30] X. Lin, J. C. Lu, Y. Shao, Y. Y. Zhang, X. Wu, J. B. Pan, L. Gao, S. Y. Zhu, K. Qian, Y. F. Zhang, D. L. Bao, L. F. Li, Y. Q. Wang, Z. L. Liu, J. T. Sun, T. Lei, C. Liu, J. O. Wang, K. Ibrahim, D. N. Leonard, W. Zhou, H. M. Guo, Y. L. Wang, S. X. Du, S. T. Pantelides, H. J. Gao, *Nat. Mater.* **2017**, *16*, 717.

[31] A. Winkelmann, C. Tusche, A. Akin Ünal, M. Ellguth, J. Henk, J. Kirschner, *New J. Phys.* **2012**, *14*, 043009.

[32] B. Feng, B. Fu, S. Kasamatsu, S. Ito, P. Cheng, C. C. Liu, Y. Feng, S. Wu, S. K. Mahatha, P. Sheverdyaeva, P. Moras, M. Arita, O. Sugino, T. C. Chiang, K. Shimada, K. Miyamoto, T. Okuda, K. Wu, L. Chen, Y. Yao, I. Matsuda, *Nat. Commun.* **2017**, *8*, 1007.

[33] Q. Tong, H. Yu, Q. Zhu, Y. Wang, X. Xu, W. Yao, *Nat. Phys.* **2017**, *13*, 356.

[34] G. Kresse, J. Furthmüller, *Phys. Rev. B* **1996**, *54*, 11169.

[35] G. Kresse, J. Furthmüller, *Comput. Mater. Sci.* **1996**, *6*, 15.

[36] D. M. Ceperley, B. J. Alder, *Phys. Rev. Lett.* **1980**, *45*, 566.

[37] J. T. Sun, Z. F. Wang, S. Meng, S. X. Du, F. Liu, H. J. Gao, *2D Mater.* **2016**, *3*, 035026.

[38] I. Souza, N. Marzari, D. Vanderbilt, *Phys. Rev. B* **2001**, *65*, 035109.

[39] H. Fu, Z. Liu, C. Lian, J. Zhang, H. Li, J.-T. Sun, S. Meng, *Phys. Rev. B* **2016**, *94*, 035427.

[40] N. Marzari, D. Vanderbilt, *Phys. Rev. B* **1997**, *56*, 12847.

[41] A. Togo, F. Oba, I. Tanaka, *Phys. Rev. B* **2008**, *78*, 134106.

[42] K. Parlinski, Z. Q. Li, Y. Kawazoe, *Phys. Rev. Lett.* **1997**, *78*, 4063.

[43] A. Togo, I. Tanaka, *Scr. Mater.* **2015**, *108*, 1.

[44] I. Horcas, R. Fernandez, J. M. Gomez-Rodriguez, J. Colchero, J. Gomez-Herrero, A. M. Baro, *Rev. Sci. Instrum.* **2007**, *78*, 013705.